Phase-modulated continuous-wave coherent ranging method for optical phased array lidar

ZHANG MINGSHI,[1,2] WANG YUBING,[1,*] ⓘ ZHANG LANXUAN,[3] HU QIAN,[4] ZHAO SHUHUA,[1,2] LIANG LEI,[1] CHEN YONGYI,[1] QIN LI,[1] SONG JUNFENG,[3,5] AND WANG LIJUN[1,3]

[1] *State Key Laboratory of Luminescence and Applications, Changchun Institute of Optics, Fine Mechanics and Physics, Chinese Academy of Sciences, Changchun 130033, China*
[2] *Center of Materials Science and Optoelectronics Engineering, University of Chinese Academy of Sciences, Beijing 100049, China*
[3] *Peng Cheng Laboratory, Shenzhen 518000, China*
[4] *School of Mathematics and Statistics, Changchun University of Technology, Changchun 130012, China*
[5] *State Key Laboratory on Integrated Optoelectronics, College of Electronic Science and Engineering, Jilin University, Changchun 130012, China*
*wangyubing@ciomp.ac.cn

Abstract: Light detection and ranging (lidar) is widely accepted as an indispensable sensor for autonomous vehicles. There are two fundamental challenges in a lidar system: optical beam steering technique and ranging method. Optical phased array (OPA) is considered as one of the most promising beam steering schemes due to its solid state, compact size, and high reliability. As for ranging method, time-of-flight and frequency-modulate continuous-wave (FMCW) are commonly utilized in numerous research. However, they are impractical to commercial OPA lidar due to either requiring excessive optical power or the poor stability, high complexity, and high insertion loss of the FMCW source. As a result, the development of OPA lidars is significantly hindered by the lack of a feasible ranging method. In this paper, we present a phase-modulated continuous-wave (PhMCW) ranging method with excellent ranging accuracy and precision. Ranging error as low as 0.1 cm and precision on the order of 3.5 cm are achieved. In addition, theoretical and experimental study on simultaneous velocity measurement is carried out and velocity error as low as 0.15 cm/s is obtained. Finally, we develop a proof-of-concept OPA-PhMCW lidar and obtain a point cloud with excellent fidelity. Our work paves a novel approach to solid-state, cost-effective and high-performance OPA lidars.

1.   Introduction

It's been widely accepted in scientific community that light detection and ranging (lidar) is indispensable for autonomous vehicle due to its long range, superior accuracy and high angular resolution [1–17], compared with its counterpart operating at radio frequency. Optical beam steering and ranging are two fundamental challenges in a lidar [4]. Among various beam steering approaches, optical phased array (OPA) is regarded as one of the most promising solid-state beam steering technology due to its compact size, high reliability and compatibility to CMOS fabrication technology [2,4–10,18–24]. Much effort has been made to improve performances of OPA including field of view (FOV) [8,10,18–20], beam divergence [9,10,21], steering speed [7,22] and power efficiency [7,21–23]. Recently, state-of-the-art OPA achieves aliasing-free 180-degree FOV and beam divergence as low as 0.08 degree, applicable to autonomous vehicles [18].

As for the ranging mechanism, time-of-flight (ToF) is one of the most popular ranging methods. Hyunil Byun *et al*. demonstrated 3D depth scan up to 20 m using a ToF system accompanied with an OPA chip [4]. Zhang *et al*. also developed an OPA-ToF lidar capable of 20-m ranging

[9]. However, due to strong two-photon absorption in OPA chips, the peak transmitting power is limited to 720 mW [8], which is two orders of magnitude lower than that required to detect a target locating at hundreds of meters. Therefore, long-range OPA lidar based on ToF method is theoretically infeasible. As a result, more recent research interest moves on to frequency-modulate continuous-wave (FMCW) method [2,6,9–13,15] due to relaxed requirement for optical power, low electronic bandwidth, simultaneous measurement of distance and velocity and intrinsic rejection to ambient light. C.V. Poulton *et al.* for the first time developed an OPA-FMCW lidar operating at a range of 185 m [7]. Li *et al.* embed an OPA into a FMCW system and achieved 100-m distance measurement [10]. Although FMCW sources based on pre-distortion [11–13], optical phase-locked loop [14], IQ modulator [15,25] and self-injection locking [26] have been developed, they generally suffer from low stability, high system complexity and high insertion loss, making them impractical to commercial applications.

In this paper, phase-modulated continuous-wave (PhMCW) ranging method is proposed, through which distance information is demodulated from the time-varying optical phase. Firstly, theoretical study on the PhMCW ranging mechanism is carried out. Moreover, excellent accuracy and precision of the PhMCW method are experimentally demonstrated. Ranging error as low as 0.1 cm and precision on order of 3.5 cm are achieved. A modified precision model is proposed as well. Furthermore, theoretical and experimental study on simultaneous velocity measurement is carried out. Velocity error as low as 0.15 cm/s is achieved. Finally, a proof-of-concept OPA-PhMCW lidar is developed and point cloud with exceptional 3D fidelity is obtained. Our work also paves a novel way approaching to solid-state, cost-effective and high performance OPA lidars.

2.   Phase-modulated continuous-wave ranging mechanism

Light is electromagnetic field operating at optical frequency [27]. Conventional ranging methods, such as ToF and FMCW, acquire ranging results via amplitude and frequency modulation [1–13,15,18,28], respectively, whereas optical phase is generally considered constant. However, time-varying phase can be utilized to demodulate timing information as well.

The mechanism of the proposed PhMCW method is illustrated in Fig. 1. The laser phase $\varphi_T(t)$ is modulated by a rectangular waveform, where φ_0 is initial optical phase, $\Delta\varphi$ is modulation depth, n is an integer and T is period of phase modulation.

$$\varphi_T(t) = \begin{cases} \varphi_0, & \left(nT \le t < \frac{T}{2} + nT\right) \\ \varphi_0 + \Delta\varphi, & \left(\frac{T}{2} + nT \le t < (n+1)T\right) \end{cases} \tag{1}$$

A portion of the modulated laser is coupled as local oscillator (LO) and the rest is transmitted into free space (TX). Assuming there is no phase delay between TX and LO, the electric field of LO is $E_{LO}(t) = A_{LO}\cos[\omega_0 t + \varphi_T(t)]$, where A_{LO} is amplitude of the electric field of LO and ω_0 is optical frequency. The TX signal is back-scattered by the target and is collected by the receiver. Therefore, the received signal (RX) is a delayed and attenuated version of TX and its electric field is given by Eq. (2), where A_R is amplitude of the electric field of RX and τ is time of flight.

$$E_R(t) = A_R\cos[\omega_0(t-\tau) + \varphi_T(t-\tau)] \tag{2}$$

The RX and LO are subsequentially mixed in optical domain and intermediate frequency (IF) signal equals to the envelop of the total electric field [27], i.e., $I_{IF}(t) = \langle|E_R(t)+E_{LO}|^2\rangle_t$, where $\langle\bullet\rangle_t$ denotes to the time average of $\bullet$. Considering a stationary target, the IF signal can be expressed as Eq. (3). Please note that although there may be phase delay between LO and TX, it

is constant and has no influence on the pulse width of the IF signal.

$$I_{IF}(t) = \begin{cases} A_{LO}A_R \cos(\omega_0\tau + \Delta\varphi), & (0 + nT \leq t < \tau + nT) \\ A_{LO}A_R \cos(\omega_0\tau), & (\tau + nT \leq t < \frac{T}{2} + nT) \\ A_{LO}A_R \cos(\omega_0\tau - \Delta\varphi), & (\frac{T}{2} + nT \leq t < \frac{T}{2} + \tau + nT) \\ A_{LO}A_R \cos(\omega_0\tau), & (\frac{T}{2} + \tau + nT \leq t < (n+1)T) \end{cases} \quad (3)$$

Figure 2(a)-(d) show the simulated IF waveforms with $\omega_0 = 193.55$ THz, $\Delta\varphi = \pi/2$ and $\tau = 26.76$ ns, 26.82 ns, 23.39 ns, and 25.15 ns, respectively. Figure 2(e)-(h) are the corresponding experimentally measured IF signals. It is obvious that the IF signal is bound to be a stream of pulses whose pulse width equals to τ, although its shape transforms with τ. Therefore, we can obtain the distance information by measuring the pulse width of the IF signal and then multiply it by $c/2$, where c is the speed of light.
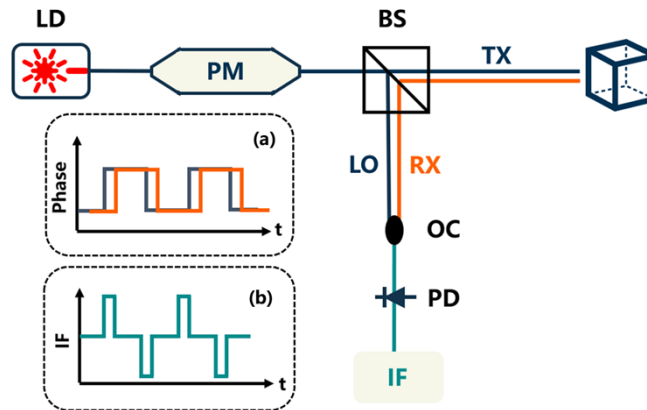

Fig. 1. Schematic of the working mechanism of the PhMCW ranging method. Inset: Waveforms of (a) optical phase of LO and RX, and (b) IF signal. LD: Laser. PM: phase modulator. BS: beam splitter. OC: optical coupler. PD: photodetector.
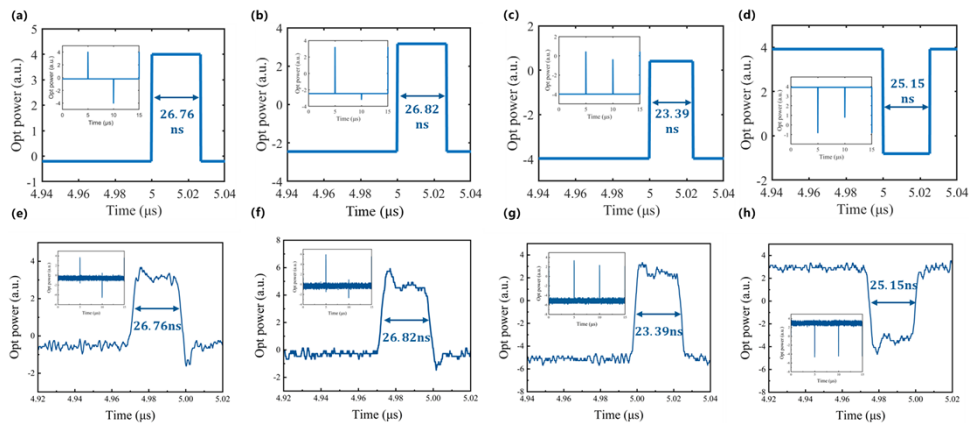

Fig. 2. (a)-(d) Simulated IF waveforms with $\tau = 26.76$ ns, 26.82 ns, 23.39 ns, and 25.15 ns respectively. (e)-(h) The corresponding experimentally measured IF signals. Insets are the zoomed-in waveforms of a single pulse.

3. Ranging experiment

In order to demonstrate the validation of the proposed PhMCW method, we built a PhMCW system based on a mono-static configuration, as shown in Fig. 3. The light source (Connect CoSF-D) is a 1550-nm CW 15-kHz-linewidth laser followed by an erbium doped fiber amplifier (Thorlabs EDFA100S). A LiNbO$_3$ phase modulator driven by an arbitrary function generator (AFG) is used to modulate the optical phase. The modulated laser is split into LO and TX by a 10:90 beam splitter. The TX signal is then collimated and emitted into free space. The received RX signal is routed to a 2×2 optical coupler, where LO and RX signals are mixed together. The mixed optical signal is converter to electrical IF signal by a pair of balanced photodetectors (Thorlabs PDB470C-AC) whose noise equivalent power is 77 pW. Finally, the IF signal is monitored, stored and digitally processed by an oscilloscope (Tektronix MSO54). The sampling interval, sampling rate and analog bandwidth of the oscilloscope are 160 ps, 6.25 Gsps, and 500 MHz, respectively, and the time window is 200 ns during time-domain analysis. The target is an off-the-shelf diffused reflection board with a reflectivity of 90%. The actual distance is measured via a commercial laser rangefinder with an accuracy of 1 mm. According to IEC 60825-1:2014 [29], the maximum permissible exposure at 1550 nm with a CW laser is 1000W/m^2. Given that the pupil range of human eye is 3-7 mm, the corresponding optical power is 7-38 mW. Therefore, the optical power at the collimator is maintained to be 10 mW. Distance to the target is varied from 1 m to a maximum of 8 m, which is limited by laboratory area.
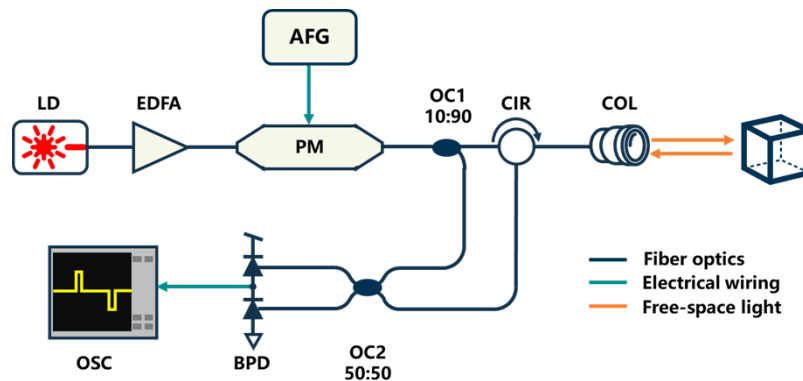

Fig. 3. Schematic of the PhMCW system. LD: Laser. EDFA: erbium doped fiber amplifier. PM: phase modulator. AFG: arbitrary function generator. OC: optical coupler. CIR: circulator. COL: collimator. BPD: balance photodetector. OSC: oscilloscope.

Figure 4 shows a typical waveform of the IF signal with the target locating at 7 m. The pulse width is 69.398 ns. Multiplying the pulse width by $c/2$, the measured distance is calculated to be 10.41 m. The discrepancy between the actual distance and the measured distance is due to that fiber optics such as circulator and fiber unintentionally introduce a phase delay between LO and RX, and therefore result in a ranging offset. In our system, the ranging offset is calibrated to be 3.41 m. The calibration process is as follows: Firstly, the measured distance is obtained by averaging the pulse widths of 20 consecutive IF signals. This excludes any influences resulting from short-term mechanical vibrations or thermal fluctuations. Then, the measured distance is linear fitted with the actual distance. The 3.41-m distance offset is obtained by the y-intercept of the linear fitting. This whole calibration process is finished as fast as possible to exclude any long-term influencing factors such as thermal variation. In the remaining of this paper, all ranging results have excluded the aforementioned ranging offset without further notice. The measured distance as function of actual distance is shown in Fig. 5. The linear relationship between the measured distance and the actual distance indicates the validation of the PhMCW method.

In addition, the minimum and maximum ranging error are 0.1 cm and 4.7 cm, respectively, suggesting excellent accuracy.

In Fig. 4, the signal level (the height of the rectangular waveform) is measured to be 71 mV and the noise level (the standard deviation of the noise floor) is measured to be 1.9 mV. Therefore, the SNR at 7 m is calculated to be 36.01. Given the SNR is proportional to the reciprocal of distance for heterodyne detection, the maximum ranging distance for the current setup is calculated to be 100.8 m assuming a reasonable SNR of 2.5. Increasing the aperture size of the receiver and reducing the bandwidth of the detectors could further increase the maximum ranging distance of the PhMCW lidar.
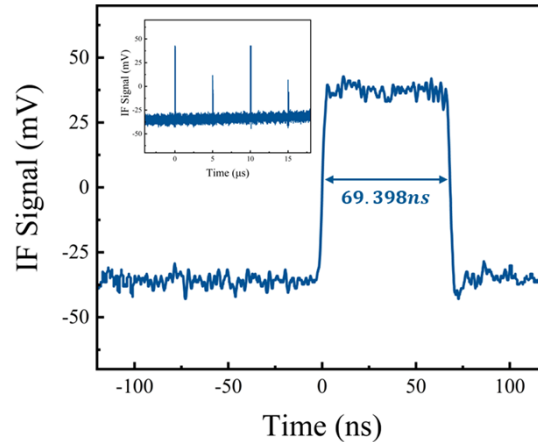

Fig. 4. Waveform of the IF signal with the target locating at 7 m. Inset: Waveform of the IF signal spanning two phase modulation period.
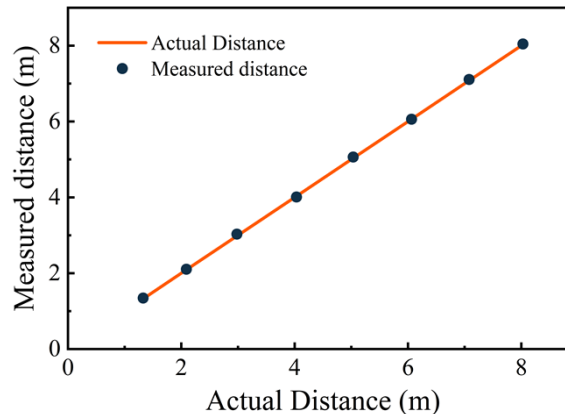

Fig. 5. Measured distance as function of actual distance.

4.   Ranging precision

So far, we have experimentally demonstrated the excellent accuracy of the PhMCW method. In addition to accuracy, precision is another important criterion. High precision is necessary [1,3,5,7] for numerus applications, such as autonomous vehicles, aerial mapping and robotics. Therefore, we will thoroughly explore the precision model of the PhMCW method.

Theoretically, ranging precision σ is inversely proportional to the square root of signal-to-noise ratio (SNR), i.e., $\sigma^2 \propto 1/SNR$ [3,30,31]. In our ranging system as shown in Fig. 3, the power of LO is on order of 1 mW, which is orders of magnitude higher than the power of RX. Therefore, the noise of the system can be reasonably believed to be dominated by the shot noise of LO, which is constant no matter what the power of RX is. On the other hand, according to Eq. (3), the IF signal level is proportional to the amplitude of the electric field of RX signal A_R, i.e., square root of the RX power $\sqrt[2]{P_{RX}}$. Assuming a Lambertian surface, power of the RX signal at normal incidence can be expressed as:

$$P_{RX} = P_{TX} \frac{\rho}{\pi} \frac{A_{RX}}{d^2} \tag{4}$$

where P_{TX} is the transmitted power, ρ is the reflectivity, A_{RX} is the area of the RX aperture and d is the distance to the target. According to Eq. (4), P_{RX} is primarily affected by ρ and d^2 [2]. Therefore, σ is derived to be proportional to $\sqrt[2]{d}$ and inversely proportional to $\sqrt[4]{\rho}$, as given by Eq. (5).

$$\sigma \propto \frac{1}{\sqrt[2]{SNR}} \propto \frac{\sqrt[2]{Noise}}{\sqrt[2]{Signal}} \propto \frac{Constant}{\sqrt[4]{P_{RX}}} \propto \frac{\sqrt[2]{d}}{\sqrt[4]{\rho}} \tag{5}$$

We conducted two sets of experiments. In the first set, the reflectivity of the target was fixed at 90% with the distance to target varying from 2 m to 8 m with a step of 1 m. In the second set, the target was located at 5 m while the reflectivity varied from 10% to 90% with a step of 20%. In each ranging measurement, we acquired about 30 successive IF signals and formed ranging distribution figures with bin size of 2 cm. The time span of each ranging measurement was within 1 ms, excluding any long-term influences on the ranging results, representing the best-case precision of the PhMCW system.

Figures 6 and 7 show the distribution figures with varying distances and reflectivity, respectively. The dashed curves indicate Gaussian fits. All of the distributions confirm to Gaussian distribution. In addition, the minimum and maximum standard deviations are 2.8 cm and 3.3 cm, respectively, demonstrating exceptional precision of the PhMCW system.
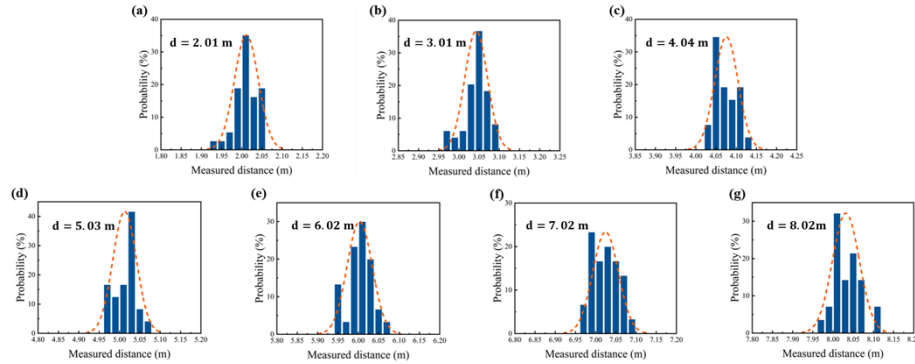

Fig. 6. Distribution figures of the ranging results with the distance to target varying from 2 m to 8 m with a step of 1 m. Dashed lines indicate Gaussian fits.

According to Eq. (5), σ is proportional to $\sqrt[2]{d}/\sqrt[4]{\rho}$ theoretically. However, considering a realistic application environment, which is neither vibration-isolated nor thermally stabilized, we modify the model of σ as given in Eq. (6), where A is a constant representing the systematic ranging jitter caused by vibrations or thermal fluctuations, and B is a coefficient representing the
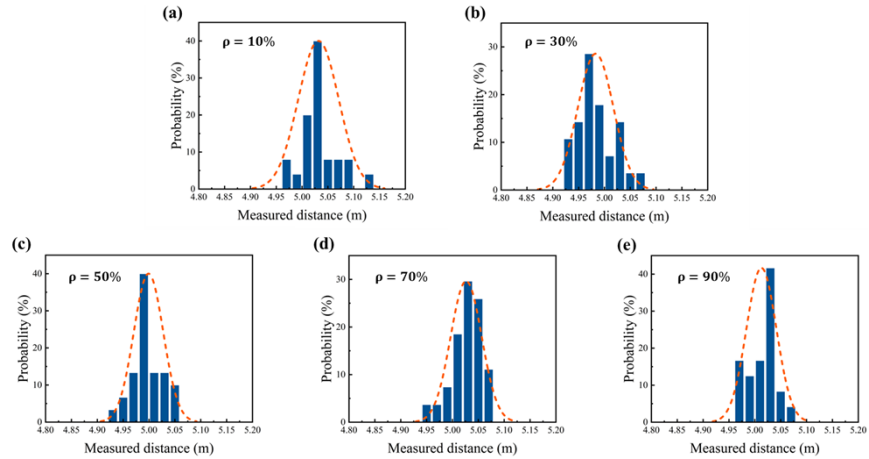
Fig. 7. Distribution figures of the ranging results with the reflectivity varied from 10% to 90% with a step of 20%. Dashed lines indicate Gaussian fits.

linear relationship between σ and $\sqrt[2]{d}/\sqrt[4]{\rho}$.

$$\sigma = A + B \times \frac{\sqrt[2]{d}}{\sqrt[4]{\rho}} \tag{6}$$

Figure 8(a) and (b) respectively illustrate precision as function of distance and reflectivity. The precision values are extracted from Figs. 6 and 7, and orange lines are fitting curves according to Eq. (6). The fitted precision formulas using data acquired from Fig. 8 (a) and (b) are $\sigma = 2.42$ cm $+ 0.27$ cm$/\sqrt[2]{m} \times \sqrt[2]{d}/\sqrt[4]{0.9}$ and $\sigma = 2.32$ cm $+ 0.24$ cm$/\sqrt[2]{m} \times \sqrt[2]{5}/\sqrt[4]{\rho}$, respectively. The relative differences of the fitted A and B are 4.1% and 12.5%, respectively. Such excellent accordance of the fitting results acquired from two independent experiments indicates the correctness of the modified model. According to such model, a vehicle with 10% reflectivity locating at 100 m would result in a precision of 6.62 cm, which is comparable to commercial lidars [16], suggesting promising application prospect of the PhMCW method.
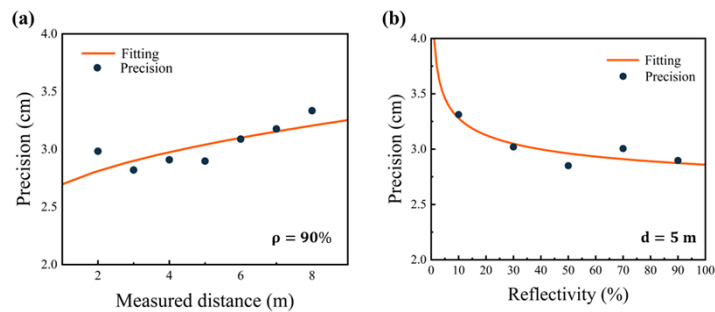

Fig. 8. Precision as function of distance (a) and reflectivity (b). Orange curves are fitting results according to Eq. (6).

5. Simultaneous velocity measurement

Simultaneous velocity measurement is also critical, since it will significantly ease post-processing algorithms such as object recognition and classification [2,6,32]. In general, ToF lidars utilize

multiple ranging frames to calculate the averaged velocity during a specific period of time. However, such multi-frame distance-differential algorithm would convert any ranging error into velocity error [33]. For example, a ToF lidar with 5 cm precision and 20 Hz frame rate may produce 1 m/s velocity error which solely originates from ranging uncertainty. This may cause failure to pedestal recognition and may result in hazardous consequences. On the other hand, coherent detection methods [2,6,33,34], such as FMCW or the proposed PhMCW, can resolve the instantaneous radial velocity by measuring the Doppler frequency, which is given by $f_d = \mathbf{k} \cdot \mathbf{v}/2\pi$, where $\mathbf{k}$ is the wave vector of incidence and $\mathbf{v}$ is the motion vector of the target [2,6,32,35]. Please note that the Doppler frequency is generally on orders of hundreds of kilohertz, which is within the spectrum range of the pronounced 1/f noise of high-speed hardware, and thus may be easily overwhelmed in noise. Furthermore, high-speed analog-to-digital converters (ADCs) are so vulnerable that high-pass analog frontends (AFEs) are generally required [36]. Therefore, the low-frequency Doppler component may also be filtered by the high-pass AFE [37,38]. Hence, simply measuring the Doppler frequency may not be adequate to analyze the instantaneous velocity, and high-frequency components of the IF spectrum must be taken into considerations as well.

   In this section, we will semi-quantitatively explore the capability of velocity measurement of the PhMCW method. According to Eq. (2), the electric field scattered off a stationary target is given by $E_R(t) = A_R \cos[\omega_0(t - \tau) + \varphi_T(t - \tau)]$. Its instantaneous frequency, which is the derivative of the phase with respect to time, equals to $\omega_0 + \varphi_T'(t - \tau)$. Taking into account the Doppler frequency, the instantaneous frequency is modified to be $\omega_0 + \omega_d + \varphi_T'(t - \tau)$, where ω_d is the Doppler frequency in radian unit. Furthermore, the phase of the RX electric field, which is the time integration of frequency, equals to $\omega_0(t - \tau) + \omega_d(t - \tau) + \varphi_T(t - \tau)$. Therefore, the IF signal for a mobile target $I_d(t)$ can be expressed as Eq. (7).

$$I_d(t) = A_{LO}A_R \cos\{-\omega_d t + \omega_0\tau + \omega_d\tau + [\varphi_T(t) - \varphi_T(t - \tau)]\} \tag{7}$$

   Since the phase of the laser is modulated by a rectangular waveform, it can be considered as the summation of the fundamental frequency component and its harmonics [39], i.e., $\varphi_T(t) = \sum_{n=1}^{\infty} a_n \cos(n\omega_m t + \varphi_n)$, where ω_m is the phase modulation frequency and n is a positive integer. By combining the general term, Eq. (7) is therefore arranged as

$$i_d(t) = A_{IF} \cos\left[\omega_d t + \sum_{-\infty}^{\infty} a_p \cos(p\omega_m t + \varphi_p)\right] \tag{8}$$

where $A_{IF} = A_{LO}A_R$ is the amplitude of the IF signal and p is an integer. By recursive method and expanding the formula by Bessel series, Eq. (8) is further arranged as

$$\begin{aligned} i_d(t) = A_0 \cos(\omega_d t) + \sum_{n=1}^{\infty} a_n \cos[(n\omega_m + \omega_d)t] + \sum_{n=1}^{\infty} b_n \sin[(n\omega_m + \omega_d)t] \\ + \sum_{n=1}^{\infty} c_n \cos[(n\omega_m - \omega_d)t] + \sum_{n=1}^{\infty} d_n \sin[(n\omega_m - \omega_d)t] \end{aligned} \tag{9}$$

where A_0, a_n, b_n, c_n, d_n are constants. For more detailed deduction, please refer to Supplement 1.

   Figure 9(a) shows an image of the experimental setup. The target is a reflective disk with a diameter of 20 cm and is driven by a precision motor rotating at a calibrated angular velocity. The radial velocity v_r sensed by the PhMCW system varies with the incident angle and can be easily calculated by $v_r = \omega d \sin \theta_i / r$, where ω is the angular velocity, d is the distance between the collimator and the center of the disk, r is the radius of the disk and θ_i is the incident angle, as shown in Fig. 9 (a).

   According to Eq. (9), when the target is stationary, the spectrum of the IF signal is composed of the fundamental frequency and its harmonics, as shown in Fig. 9 (b). Whereas, when the
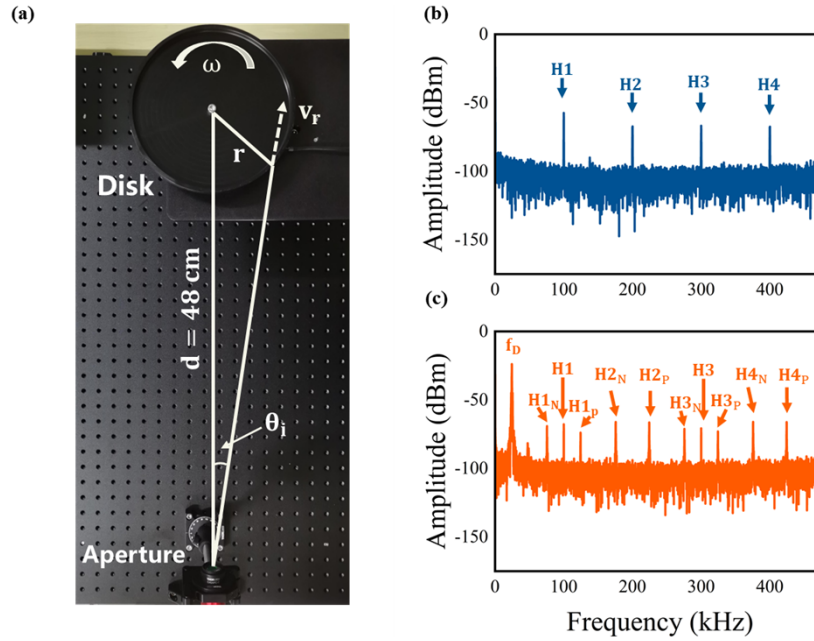
Fig. 9. (a) Image of the setup for velocity measurement. (b)-(c) Spectrum of the IF signal for a stationary target (b) and for a mobile target (c). f_d denotes the Doppler frequency. H1 denotes the fundamental frequency. H2, H3 and H4 denote the 2nd, 3rd and 4th order of harmonic, respectively. Hk_P and Hk_N represent the positive and the negative satellite peaks of the kth order of harmonic, respectively.

target is mobile, additional Doppler frequency peak appears at ω_d, and each of the fundamental and the harmonic peaks split into two satellite peaks locating at $n\omega_m \pm \omega_d$, as shown in Fig. 9 (c). The remaining fundamental and odd order of harmonics in Fig. 9 (c) is due to the residual amplitude modulation of a realistic phase modulator, since they are the spectrum components of a rectangular waveform that is used for phase modulation. The frequencies of all peaks in Fig. 9 (c) are summarized in Table 1.

Table 1. Summarization of the frequency components in the IF spectrum for a mobile target.

Peak index	f_d	$H1_N$	$H1$	$H1_P$	$H2_N$	$H2_P$	$H3_N$	$H3$	$H3_P$	$H4_N$	$H4_P$
Frequency (kHz)	24.5	75.5	100	124.5	175.5	224.5	275.5	300	324.5	375.5	424.5

As mentioned above, the low-frequency Doppler peak per se may be overwhelmed in noise or be filtered. We can also obtain the Doppler frequency by $(Hk_P - Hk_N)/2$, where Hk_P and Hk_N are frequencies of the kth pair of the satellite peaks locating at higher frequency regime. Taking the 3rd order of harmonic as an example, $H3_P$ and $H3_N$ are 324.5 kHz and 275.5 kHz, respectively, and the Doppler frequency is calculated to be 24.5 kHz, which is consistent with the frequency of the Doppler peak.

Figure 10 shows the measured radial velocity as function of incident angle. Dashed orange line indicates the calculated velocity. The velocity error ranges from -0.17 cm/s to 0.15 cm/s, suggesting exceptional velocity measurement accuracy.

The PhMCW method measures velocity based on the frequency shift of satellite peaks. The frequency shift can be resolved as long as ω_d is greater than the resolution bandwidth (RBW) of the spectrum, i.e., $2\pi/\lambda \times \Delta v_{res} = RBW$. Therefore, the radial velocity resolution is
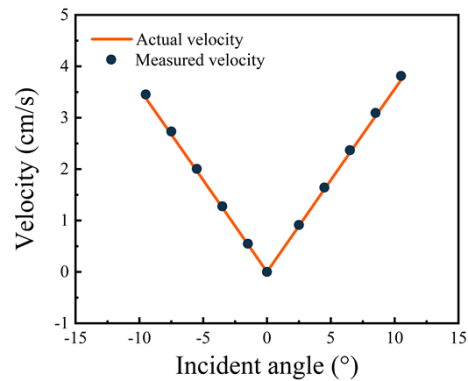
Fig. 10. Actual and measured velocity as function of incident angle.

$\Delta v_{res} = RBW \times \lambda/2\pi$, where λ is the incident wavelength. In our experiment, the RBW is set to be 100 Hz. Therefore, the velocity resolution is as low as 2.5×10^{-3} cm/s.

6. OPA PhMCW lidar

The proposed PhMCW ranging method is particularly suitable for OPA lidars since OPA chips are specialized in phase manipulation. In this section, we will perform a proof-of-concept demonstration of an OPA-PhMCW lidar.

The schematic of the OPA chip we used is illustrated in Fig. 11. The chip is fabricated on a SiN-on-SOI substrate. Laser from a lensed fiber is coupled into the SiN waveguide through an adiabatic spot-size converter (SSC). Then the input laser is split into 64 waveguides by an array of Y-branch beam splitters. Afterwards, laser is coupled to Si waveguides through vertically stacked SiN-to-Si transition couplers. Thermo-optical modulators are patterned to independently control the phase of laser in each waveguide. Finally, the Si waveguides are routed to an array of gratings through which light is emitted into free space. In the horizontal direction (θ), beam steering is achieved by controlling the phase of the optical array. In the vertical direction (φ), beam steering is achieved by changing the laser wavelength due to the dispersion property of the grating antennas.
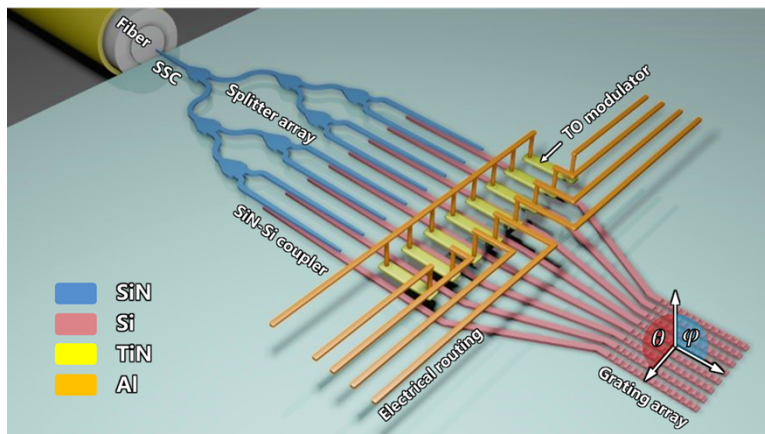

Fig. 11. Schematic of the OPA chip. For simplicity, only 8 channels are illustrated.

For a one-dimensional OPA with uniform antenna spacing, the far-field is given by $T(\theta) = \sum_{n=0}^{N-1} A_n \exp(-j\beta) \exp(-jk_0 n\Lambda \sin\theta)$, where A_n is amplitude at the nth antenna, β is phase delay between adjacent antenna, k_0 is wave vector, N is dimension of OPA and Λ is antenna spacing [40]. If optical phase at each antenna is modulated by $\varphi(t)$ simultaneously, A_n is therefore replaced by $A_n \exp[-j\varphi(t)]$. In such case, the far-field is modified to be $T_{PM}(\theta) = \sum_{n=0}^{N-1} A_n \exp[-j\varphi(t)] \exp(-j\beta) \exp(-jk_0 n\Lambda \sin\theta) = \exp[-j\varphi(t)]T(\theta)$, suggesting that not only the angle of the far-field beam is steered but also the optical phase is modulated, which is fundamental in the PhMCW ranging method. In addition, the global phase modulation can be readily achieved by integrating a phase modulator right before the beam splitter array which is shown in Fig. 11.

A global search algorithm is utilized to optimize the far-field pattern of the OPA chip by maximizing the side-lobe suppression ratio. Figure 12(a) shows images of the far-field beams steered at various θ directions. The field of view (FOV) in θ direction is 94° and the FOV in φ direction is 14.4° with laser wavelength swept from 1540 nm to 1620 nm (CoBrite DX1, linewidth = 100 kHz), as shown in Fig. 12(b). The divergence in θ and φ directions are 1.41° and 1.49°, respectively. For more detailed information of the OPA chip, please refer to our previous work [9].

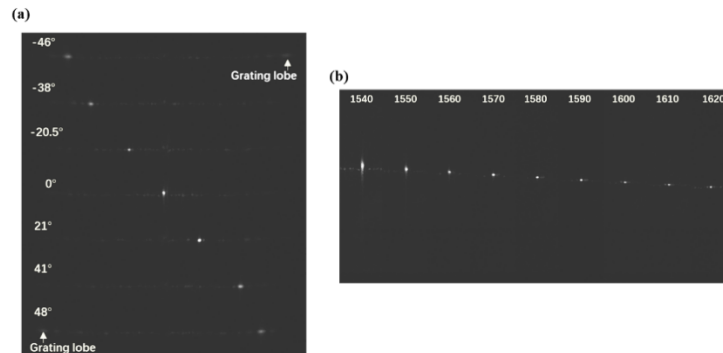**Fig. 12.** Two-dimensional beam steering in (a) θ direction and (b) φ direction.

The setup of the OPA PhMCW lidar is based on a bistatic configuration in which laser beam is emitted and steered by the OPA chip and RX signal is collected by a lens. Figure 13(a) shows a camera image of the experimental setup, including the packaged OPA module, controlling electronics, RX optics and the target. The OPA module includes the OPA chip, lensed fiber and electrical connectors packaged on a home-made printed circuit board, as shown in Fig. 13(c). The main-lobe power is estimated to be 3.5 mW. The target is composed of two letters in respective planes separated by 22.5 cm, as shown in Fig. 13(b). The reflectivity of the target is 95%. In order to achieve a 3D point cloud, the phase of the OPA and the laser wavelength are set to predetermined values. Consequently, laser beam is steered to a specific angle. At this angle, the PhMCW ranging is performed. Once we have mapped all resolvable angles, 3D point cloud is formed. The bright spots in Fig. 13(b) indicate the 2D steered laser beams. The measured point clouds are shown in Fig. 13(d). Excellent 3D image fidelity is achieved. The averaged distance of each letter are 44.16 cm and 65.48 cm, respectively. The differential distance between the letters is 21.32 cm, which is in accordance with the experimental setup.
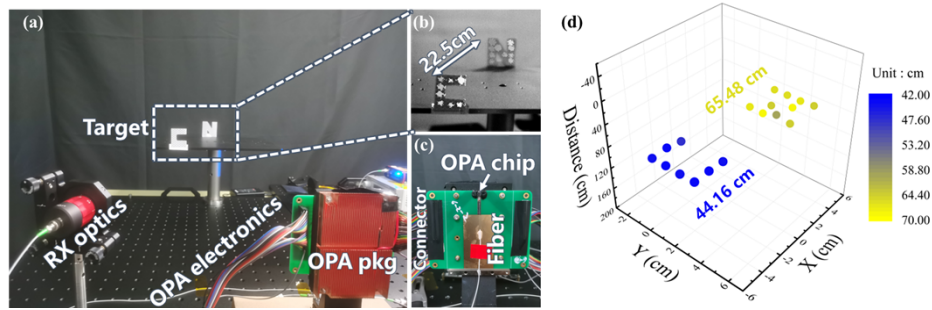
Fig. 13. (a) Image of the experiment setup. (b) Infrared image of the target. Bright spots indicate 2D steered laser beams. (c) Front image of the packaged OPA module. (d) Point clouds of the target. The point clouds are color-coded by the distance values.

7. Discussion

7.1. Maximum ranging distance and maximum velocity

According to Fig. 1, it is obvious that the maximum time of flight is half of the period of phase modulation, beyond which distance cannot be measured unambiguously. Therefore, the unambiguous range of the PhMCW method is determined by $d_{\max} = (T \times c)/4 = c/4\omega_m$. On the other hand, in order to prevent spectrum aliasing, the Doppler frequency should be lower than $\omega_m/2$ so that satellites peaks (Hk_P and Hk_N) always neighbor the corresponding harmonic Hk. Therefore, the maximum velocity is determined by $v_{\max} = (\omega_m \times c)/4\omega_0$. Consequently, there is a tradeoff between the unambiguous range and the maximum velocity. In our experiment, the phase modulation frequency is 100 kHz. The corresponding unambiguous range is calculated to be 750 m and the maximum radial velocity is 3.875 cm/s. This tradeoff can be solved by alternatively modulating the optical phase at two frequencies with the higher frequency for velocity measurement while the lower one for ranging. Alternatively, it can be solved by analyzed the velocity via the aliased spectrum in conjunction with ranging frame. The time-differentiated ranging frames provide coarse velocity range while the aliased spectrums give possible velocities with fine resolution. The one that coincides with velocity range is thus the true velocity.

7.2. Ranging resolution

Ranging resolution of the PhMCW method is theoretically determined by the timing resolution of the receiver. In our experiment, the sampling interval of the oscilloscope is 160 ps, which corresponds to a ranging resolution of 2.4 cm. However, the ranging resolution is rarely determined by the timing resolution practically. Even when we are measuring a stationary target, the measured distance jitters due to random noise. If the distance between two targets is so large that the measured distances of the two targets do not overlap, the two target can be resolved in a single ranging frame. On the contrary, similar to the Rayleigh Criterion in optics system, if the distance between two targets is smaller than precision, the two target cannot be resolved since we cannot distinguish the measured distance difference results from ranging jitter or real distance difference.

7.3. Effect of phase noise on maximum detection range

When considering the optical phase noise, the electric field of LO can be written as $E_{LO} = \cos[\omega_0 t + \varphi_m(t) + \varphi_n(t)]$, where $\varphi_m(t)$ is the modulated optical phase and $\varphi_n(t)$ is the zero-mean gaussian-distributed optical phase noise. Ignoring the DC term, the IF signal can be written as $i_{IF} = A\cos[\omega_0 \tau + \Delta\varphi_m(t, \tau) + \Delta\varphi_n(t, \tau)]$, where τ is the time-of-flight, $\Delta\varphi_m(t, \tau)$ is a stream of

pulses as shown in Fig. 1(b) and $\Delta\varphi_n(t,\tau)$ is the accumulated phase noise difference. When τ is smaller than the coherence time, $\Delta\varphi_n(t,\tau)$ is much smaller than $\Delta\varphi_m(t,\tau)$. Therefore, the optical phase noise has negligible influence on the IF pulse width. As τ increases, $\Delta\varphi_n(t,\tau)$ increases as well. The presence of phase noise adds jitters to the IF signal and consequently degrades the ranging precision.

The PhMCW ranging method resembles phase-shift keying (PSK). In PSK optical communication, data transmission over distance exceeding the coherence length is feasible. Therefore, the PhMCW ranging method will function properly even when the round-trip distance is greater than the coherence length of the laser source, as opposed to the FMCW ranging method.

7.4. Differences between AMCW and PhMCW

The electric field of light is expressed as $E = A\cos[\omega t + \varphi_{opt}]$, where A is the amplitude, ω is the frequency and φ_{opt} is the optical phase. Optical power is proportional to envelop of the electric field. Therefore, the modulation of optical power is essentially the modulation of the amplitude.

ToF ranging method modulates the transmitted optical power. For example, amplitude-modulated continuous-wave (AMCW) method modulates the optical power in sine- or rectangular fashion. The phase of the optical power φ_{pwr} of reflected signal is compared with that of the local oscillator. The phase difference of optical power $\Delta\varphi_{pwr}$ is used to estimate distance [41–43]. Please note that the "phase" throughout this paper is the optical phase φ_{opt}. The optical power of the PhMCW method is constant.

Although AMCW ranging method can reach high precision, the maximum ranging distance is limited by the power of laser source. Ranging as long as 100 m would require prohibitively high power. Therefore, AMCW method is popular for short-range applications such as smart phones, robotics, etc. One the other hand, the PhMCW method modulates the optical phase φ_{opt} while the optical power is constant (10 mW in our experiment). The local oscillator acts as an amplifier and therefore long-range distancing can be achieved.

8. Conclusions

In conclusion, we have proposed the phase-modulated continuous-wave (PhMCW) ranging method. Ranging error as low as 0.1 cm and precision on order of 3.5 cm are achieved. Moreover, we modified the precision model. In addition, theoretical and experimental study on simultaneous velocity measurement is carried out and the velocity error as low as 0.15 cm/s is obtained. Finally, we developed a proof-of-concept OPA-PhMCW lidar and achieved point cloud with exceptional 3D fidelity. The PhMCW method paves a new way approaching solid-state, cost-effective and high performance OPA lidars.

Disclosures. The authors declare no conflicts of interest.

Data availability. Data underlying the results presented in this paper are available in Dataset 1, Ref. [44].

Supplemental document. See Supplement 1 for supporting content.

References

1. X. Zhang, K. Kwon, J. Henriksson, J. Luo, and M. C. Wu, "A large-scale microelectromechanical-systems-based silicon photonics LiDAR," Nature **603**(7900), 253–258 (2022).
2. C. V. Poulton, A. Yaacobi, D. B. Cole, M. J. Byrd, M. Raval, D. Vermeulen, and M. R. Watts, "Coherent solid-state LIDAR with silicon photonic optical phased arrays," Opt. Lett. **42**(20), 4091–4094 (2017).
3. B. Behroozpour, P. A. M. Sandborn, M. C. Wu, and B. E. J. I. C. M. Boser, "Lidar System Architectures and Circuits," IEEE Commun. Mag. **55**(10), 135–142 (2017).
4. H. Byun, J. Lee, B. Jang, C. Lee, and K. Ha, "A gain-enhanced silicon-photonic optical phased array with integrated O-band amplifiers for 40-m ranging and 3D scan," in *CLEO: Science and Innovations*, (2020).

5. J. W. Shi, J. I. Guo, M. Kagami, P. Suni, and O. Ziemann, "Photonic technologies for autonomous cars: feature introduction," Opt. Express **27**(5), 7627–7628 (2019).
6. C. Rogers, A. Y. Piggott, D. J. Thomson, R. F. Wiser, I. E. Opris, S. A. Fortune, A. J. Compston, A. Gondarenko, F. Meng, X. Chen, G. T. Reed, and R. Nicolaescu, "A universal 3D imaging sensor on a silicon photonics platform," Nature **590**(7845), 256–261 (2021).
7. C. V. Poulton, M. J. Byrd, P. Russo, E. Timurdogan, M. Khandaker, D. Vermeulen, and M. R. Watts, "Long-Range LiDAR and Free-Space Data Communication With High-Performance Optical Phased Arrays," IEEE J. Sel. Top. Quantum Electron. **25**(5), 1–8 (2019).
8. L. Zhang, Y. Li, Y. Hou, Y. Wang, M. Tao, B. Chen, Q. Na, Y. Li, Z. Zhi, X. Liu, X. Li, F. Gao, X. Luo, G. Q. Lo, and J. Song, "Investigation and demonstration of a high-power handling and large-range steering optical phased array chip," Opt. Express **29**(19), 29755–29765 (2021).
9. L. Zhang, Y. Li, B. Chen, Y. Wang, H. Li, Y. Hou, M. Tao, Y. Li, Z. Zhi, X. Liu, X. Li, Q. Na, Q. Xie, M. Zhang, X. Li, F. Gao, X. Luo, G. Q. Lo, and J. Song, "Two-dimensional multi-layered SiN-on-SOI optical phased array with wide-scanning and long-distance ranging," Opt. Express **30**(4), 5008–5018 (2022).
10. Y. Li, B. Chen, Q. Na, Q. Xie, M. Tao, L. Zhang, Z. Zhi, Y. Li, X. Liu, X. Luo, G. Lo, F. Gao, X. Li, and J. Song, "Wide-steering-angle high-resolution optical phased array," Photonics Res. **9**(12), 2511–2518 (2021).
11. X. Zhang, J. Pouls, and M. C. Wu, "Laser frequency sweep linearization by iterative learning pre-distortion for FMCW LiDAR," Opt. Express **27**(7), 9965–9974 (2019).
12. G. Zhang, Z. Ding, K. Wang, Q. Lu, and W. Guo, "High output power DBR laser for FMCW LiDAR system," in *2022 Optical Fiber Communications Conference and Exhibition (OFC)*, (2022), 1–3.
13. T. H. Chen, C. Y. Huang, T. K. Shia, S. J. Wun, C. H. Hsu, K. N. Ku, C. S. Lee, C. Y. Lin, P. C. Chang, C. C. Wang, S. C. Chen, C. C. Lin, and C. I. Wu, "A Frequency Digital Pre-Distortion Compensation Method for FMCW LiDAR System," in *2020 Optical Fiber Communications Conference and Exhibition (OFC)*, (2020), 1–3.
14. A. Binaie, S. Ahasan, and H. Krishnaswamy, "A 65 nm CMOS Continuous-Time Electro-Optic PLL (CT-EOPLL) with Image and Harmonic Spur Suppression for LIDAR," in *2019 IEEE Radio Frequency Integrated Circuits Symposium (RFIC)*, (2019),
15. M. Kamata, Y. Hinakura, and T. Baba, "Carrier-Suppressed Single Sideband Signal for FMCW LiDAR Using a Si Photonic-Crystal Optical Modulators," J. Lightwave Technol. **38**(8), 2315–2321 (2020).
16. A. Carballo, J. Lambert, A. Monrroy-Cano, D. R. Wong, P. Narksri, Y. Kitsukawa, E. Takeuchi, S. Kato, and K. Takeda, "LIBRE: The Multiple 3D LiDAR Dataset," (2020).
17. S. J. P. Pan, "Coherent Random-Modulated Continuous-Wave LiDAR Based on Phase-Coded Subcarrier Modulation," Photonics **8**(11), 475 (2021).
18. Y. Liu and H. Hu, "Silicon optical phased array with a 180-degree field of view for 2D optical beam steering," Optica **9**(8), 903–907 (2022).
19. P. Wang, G. Luo, Y. Li, W. Yang, H. Yu, X. Zhou, Y. Zhang, and J. Pan, "Large scanning range optical phased array with a compact and simple optical antenna," Microelectron. Eng. **224**, 111237 (2020).
20. J. Midkiff, K. M. Yoo, J.-D. Shin, H. Dalir, M. Teimourpour, and R. T. Chen, "Optical phased array beam steering in the mid-infrared on an InP-based platform," Optica **7**(11), 1544–1547 (2020).
21. P. Wang, G. Luo, Y. Xu, Y. Li, Y. Su, J. Ma, R. Wang, Z. Yang, X. Zhou, Y. Zhang, and J. Pan, "Design and fabrication of a SiN-Si dual-layer optical phased array chip," Photonics Res. **8**(6), 912–919 (2020).
22. X. Li, L. Lu, W. Gao, X. Li, J. Chen, and L. Zhou, "Silicon non-blocking 4 × 4 optical switch with automated polarization adjustment," Chin. Opt. Lett. **19**(10), 101302 (2021).
23. S. A. Miller, Y.-C. Chang, C. T. Phare, M. C. Shin, M. Zadka, S. P. Roberts, B. Stern, X. Ji, A. Mohanty, O. A. Jimenez Gordillo, U. D. Dave, and M. Lipson, "Large-scale optical phased array using a low-power multi-pass silicon photonic platform," Optica **7**(1), 3–6 (2020).
24. N. Dostart, B. Zhang, A. Khilo, M. Brand, K. Al Qubaisi, D. Onural, D. Feldkhun, K. H. Wagner, and M. A. Popović, "Serpentine optical phased arrays for scalable integrated photonic lidar beam steering," Optica **7**(6), 726–733 (2020).
25. P. Shi, L. Lu, C. Liu, G. Zhou, W. Xu, J. Chen, and L. Zhou, "Optical FMCW Signal Generation Using a Silicon Dual-Parallel Mach-Zehnder Modulator," IEEE Photonics Technol. Lett. **33**(6), 301–304 (2021).
26. E. A. Kittlaus, D. Eliyahu, S. Ganji, S. Williams, A. B. Matsko, K. B. Cooper, and S. Forouhar, "A low-noise photonic heterodyne synthesizer and its application to millimeter-wave radar," Nat. Commun. **12**(1), 4397 (2021).
27. B. van Oosten, K. Schoenmaker, and R. J. Science, "Probing the magnetic field of light at optical frequencies," Science **326**(5952), 550–553 (2009).
28. X. Sun, L. Zhang, Q. Zhang, and W. Zhang, "Si Photonics for Practical LiDAR Solutions," Appl. Sci. **9**(20), 4225 (2019).
29. "Working with lasers Updated to include IEC :2014," retrieved https://slideplayer.com/slide/12202834/.
30. K. Thurn, R. Ebelt, and M. Vossiek, "Noise in Homodyne FMCW radar systems and its effects on ranging precision," in *Microwave Symposium Digest (IMS)*, (2013 IEEE MTT-S International, 2013).
31. P. M. J. A. Woodward and N. H. Analysis, "Probability and Information Theory," **41**, 59–68 (1953).
32. Z. Xu, L. Tang, H. Zhang, and S. Pan, "Simultaneous Real-Time Ranging and Velocimetry via a Dual-Sideband Chirped Lidar," IEEE Photonics Technol. Lett. **29**(24), 2254–2257 (2017).
33. M. M. Bayer, X. Li, G. N. Guentchev, R. Torun, J. E. Velazco, and O. Boyraz, "Single-shot ranging and velocimetry with a CW lidar far beyond the coherence length of the CW laser," Opt. Express **29**(26), 42343–42354 (2021).

34. J. T. Spollard, L. E. Roberts, C. S. Sambridge, K. McKenzie, and D. A. Shaddock, "Mitigation of phase noise and Doppler-induced frequency offsets in coherent random amplitude modulated continuous-wave LiDAR," Opt. Express **29**(6), 9060–9083 (2021).

35. M. U. Piracha, D. Nguyen, I. Ozdur, and P. J. Delfyett, "Simultaneous ranging and velocimetry of fast moving targets using oppositely chirped pulses from a mode-locked laser," Opt. Express **19**(12), 11213–11219 (2011).

36. T. INSTRUMENTS, "ADC10D1000/ADC10D1500 Low Power, 10-Bit, Dual 1.0/1.5 GSPS or Single 2.0/3.0 GSPS ADC," retrieved www.ti.com.

37. T. INSTRUMENTS, "OPA859 1.8 GHz Unity-Gain Bandwidth, 3.3-nV/√Hz, FET Input Amplifier," retrieved www.ti.com.

38. T. Instruments, "WIDEBAND FIXED-GAIN AMPLIFIER," retrieved www.ti.com.

39. C.-C. Huang, T.-L. Tsai, Y.-C. Hsieh, and H.-J. Chiu, "A Bilateral Zero-Voltage Switching Bidirectional DC-DC Converter with Low Switching Noise," Energies **11**(10), 2618 (2018).

40. K. Van Acoleyen, H. Rogier, and R. J. O. E. Baets, "Two-dimensional optical phased array antenna on silicon-on-insulator," Opt. Express **18**(13), 13655 (2010).

41. I.-G. Jang, S.-H. Lee, and Y.-H. Park, "A Parallel-Phase Demodulation-Based Distance-Measurement Method Using Dual-Frequency Modulation," Appl. Sci. **10**(1), 293 (2019).

42. R. Whyte, L. Streeter, M. J. Cree, and A. A. Dorrington, "Application of lidar techniques to time-of-flight range imaging," Appl. Opt. **54**(33), 9654–9664 (2015).

43. S.-H. Lee, W.-H. Kwon, Y.-S. Lim, and Y.-H. Park, "Highly precise AMCW time-of-flight scanning sensor based on parallel-phase demodulation," Measurement **203**, 111860 (2022).

44. M. Zhang, "Phase-modulated continuous-wave coherent ranging method for optical phased array Lidar," retrieved https://doi.org/10.6084/m9.figshare.21701609.